Fracturing Process Analysis of the Beishan granite Based on Acoustic Emission and Strain Energy under True Triaxial Compression

Yan Zhang[a], Xia-Ting Feng[a,*], Chengxiang Yang[a], Xiwei Zhang[a], Mostafa Sharifzadeh[b], Zhaofeng Wang[c]

[a] Key Laboratory of Ministry of Education on Safe Mining of Deep Metal Mines, Northeastern University, Shenyang 110819, China

[b] Department of Mining Engineering, Western Australian School of Mines (WASM), Curtin University, Kalgoorlie, Australia

[c] State Key Laboratory of Geomechanics and Geotechnical Engineering, Institute of Rock and Soil Mechanics, Chinese Academy of Sciences, Wuhan 430071, China

* Corresponding author

Email: xtfeng@whrsm.ac.cn; xia.ting.feng@gmail.com (Xia-Ting Feng)

Abstract

The study of rock fracturing is a fundamental research in rock mechanics and engineering. In this paper, based on the complete stress–strain curves under TTC, the corresponding AE and strain energy results, the mechanical properties and fracturing process of the Beishan granite are studied. A representative test result (σ_2=75 MPa, σ_3=20 MPa) is selected to analyse and illustrate the three-dimensional fracturing process of the Beishan granite. The results show that the variations in the brittle fracture behaviours, AE and strain energy characteristics of the Beishan granite change with σ_2 or σ_3 following certain relationships and the mechanisms driving these various relationships are very different. The AE and strain energy characteristics during the five fracturing evolution stages of the Beishan granite are also quite different. The variations of the increments of AE count, AE event and total elastic strain energy per unit time ($\Delta S_c/\Delta t$, $\Delta S_e/\Delta t$ and $\Delta U_e/\Delta t$) are mainly studied with the different time and stress level during the rock failure. The rock fracturing evolution process can be illustrated with deep insight through the variation of these parameters. This research gives a perspective to study the deep underground fracture formation processes such as earthquake, tunnel sudden failure, spalling, splitting and rockburst.

Keywords: Fracturing process; Acoustic emission; Strain energy; Beishan granite; True triaxial compression

1. Introduction

The occurrence of hazards in natural and engineered cases such as spalling and rockburst in deep underground rock engineering is related to the evolution of the true triaxial stress field ($\sigma_1 > \sigma_2 > \sigma_3$) in which the rock mass is located.[1] Research on the fracturing of deep rock masses by laboratory true triaxial testing is quite helpful for studying the evolution and mechanisms of various hazards.[2-4] Many research methods have been applied to study this problem. However, due to the limitations of observation techniques and methods, it is still more difficult to monitor and quantify the initial position of micro-cracks inside a rock and thus the dynamic evolution of cracks.

Acoustic emission (AE) can directly reflect the internal damage of rock during the evolution of deformation and failure.[5,6] The relationships of the AE characteristic parameters that change with time and stress can visually express the crack initiation rate in rock at different damage development stages. The AE hypocenter location technique can stereoscopically show the spatial location, spatial morphology, initiation rate and propagation direction of cracks. [7-10] Many applications of the AE technique have been carried out in rock studies, mainly focusing on four aspects: the AE time series,[11] AE spectrum characteristics,[12] AE spatial distribution[13] and AE mechanism.[14] AE has been proven to be one of the best ways to study dynamic crack propagation.

By utilizing strain energy theory, the rock fracturing process can be totally analysed and interpreted.[15,16] The energy evolution mechanism is closely related to the micro-cracking and damage state inside the rock. The rock fracturing is a process of energy input, elastic strain energy accumulation, energy dissipation and energy release.[17,18] Most of the research on strain energy is focused on three aspects about the experiments study of energy evolution process and characteristic,[19] energy-based constitutive relations, criteria and index,[20] numerical simulation of energy evolution.[21]

In this study, a series of true triaxial compression (TTC) tests of the Beishan granite are carried out. Some tests are monitored by AE, and strain energy analysis is also used to study the test results. Furthermore, the stress–strain relationship, AE and strain energy characteristics of the Beishan granite under different TTC stress states are studied. The spatial fracture evolution of a representative test result are also investigated. This research offers a helpful insight to internal mechanism of rock fracturing and hazards formation and possible timely prevention.

2. Methodology

2.1. Rock description and specimen preparation

The Beishan area is located in Gansu Province in Northwestern China, which has been preliminarily chosen as the preferred area for China's potential high-level radioactive nuclear waste (HLW) repository.[22,23] The Beishan granite tested in this study is medium- to coarse-grained monzonitic granite with relatively good isotropy (Fig. 1). Some basic physical and mechanical properties of the tested Beishan granite are presented in Table 1.

The specimens of the Beishan granite used in the TTC tests are rectangular prisms with dimensions of 50×50×100 mm^3. The flatness and roughness of the specimen ends are controlled to no more than 10 μm and 3 μm, respectively. The tolerances for the end surface dimensionality and perpendicularity are limited no more than ±0.01 and ±0.02 mm, respectively. To reduce the experimental error and the differences among the specimens, all the specimens are taken from the same block of granite rock and in a consistent sampling direction.

2.2. Testing apparatus and methods

The TTC tests in this study are performed using the novel true triaxial testing apparatus at Northeastern University in China. The deformations in the ε_1 and ε_2 directions are measured by mini linear variable differential transformers (LVDTs), and the deformations in the ε_3 directions are measured by a beam type strain gauge, which can determine the centre point of the deformation of the specimen in the ε_3 direction. A series of anti-friction measures are adopted, and the friction coefficient is reduced to 0.02.[24] Detailed descriptions of the true triaxial testing apparatus can be found in Feng et al.[2] The PCI-2 AE system is also used during the TTC tests in this study. Improved high-frequency and anti-pressure AE sensors are developed, to make the AE signal as much as possible and the noise as little as possible, the AE amplitude threshold is finally selected to be 45 dB. Because the rock specimen is covered by four metal fixtures in the σ_1 and σ_2 directions, the AE sensors can be mounted on only the two specimen faces in the σ_3 direction. Eight AE sensors are mounted on these two faces of the specimen; the distribution of the AE sensors is shown in Fig. 2.

The stress paths used for the TTC tests in this study are as follows (Fig. 3): At the beginning of the test, σ_1, σ_2 and σ_3 are simultaneously loaded to the preset σ_3 value at a rate of 0.5 MPa/s. Then, σ_3 is kept constant, while σ_1 and σ_2 are simultaneously loaded to the preset σ_2 value at a rate of 0.5 MPa/s. Finally, σ_2 and σ_3 are kept constant, while σ_1 is loaded at a rate of 0.5 MPa/s; when σ_1 approaches the damage stress σ_{cd}, the loading method is changed to load σ_1 with a rate of 0.015 mm/min in ε_3 until the rock specimen failure.

3. Experimental Results

3.1. Stress–strain relationships of the Beishan granite under TTC

The strength and deformation properties of rocks under various true triaxial stress conditions are diverse. Fig. 4 shows the variation in the stress–strain relationships of the Beishan granite with different σ_2 values under TTC. When σ_3 is constant (σ_3=5 MPa) and the σ_2 values are set to 20 MPa, 75 MPa, 100 MPa and 150 MPa, the peak strengths (σ_1) of the Beishan granite are 267.8 MPa, 300.4 MPa, 316.1 MPa and 281.9 MPa, respectively, while the peak strains (ε_1) are 0.68 %, 0.62 %, 0.58 % and 0.36 %, respectively (Fig. 4). Therefore, under TTC stress state, the rock failure strength first increases and then decreases with increasing σ_2, and the peak strain of the rock decreases with increasing σ_2, which is consistent with previous research results.[2,25,26] Results also shows that, with the increase in σ_2, the rock tends to experience brittle failure (Class II failure), and the stress drop at post-peak of the stress–strain curve is more obvious, which indicates that an increase in σ_2 makes the rock more inclined to brittle failure. In addition, with the increase in σ_2, the σ_1–ε_2 curve and the σ_1–ε_3 curve of the rock become increasingly bifurcated, that is, the difference between ε_2 and ε_3 increases with increasing σ_2. Therefore, under TTC stress state, the control of σ_2 on rock deformation is very important; the larger the difference between σ_2 and σ_3 is, the greater the difference between ε_2 and ε_3.

Fig. 5 shows the variation in the stress–strain relationships of the Beishan granite with different σ_3 values under TTC. We found that when σ_2 is constant (σ_2=75 MPa) and the σ_3 values are 5 MPa, 10 MPa, 20 MPa and 30 MPa, respectively, the peak strengths (σ_1) of the Beishan granite are 300.4 MPa, 353.4 MPa, 437.1 MPa and 495.9 MPa, respectively, and the peak strains (ε_1) are 0.62 %, 0.75 %, 0.81 % and 0.9 %, respectively (Fig. 5). Therefore, the rock failure strength and peak strain increase with increasing σ_3 under TTC conditions. The rock ductility

(Class I failure) tends to increase with increasing σ_3, indicating that an increase in σ_3 weakens the rock brittleness. Moreover, comparison of Fig. 5a to Fig.5d shows that, when σ_3 is increased by 25 MPa, the failure strength of the rock is increased by 195.5 MPa. However, comparison of Fig. 4c with Fig. 4a reveals that, when σ_2 is increased by 80 MPa, the failure strength of the rock is increased by only 48.3 MPa. Therefore, the influence of σ_3 on the strength of the Beishan granite is much greater than the corresponding influence of σ_2.

3.2. Strain energy characteristic of the Beishan granite under TTC

Firstly, it should be declared that the strain energy in this paper actually means the strain energy density. When calculating the strain energy under TTC, for any time step t during the test, the total strain energy U of rock can be calculated through Eq. (1),[27-29] as shown in follows:

$$U=U_1+U_2+U_3=\int_0^{\varepsilon_1^t}\sigma_1 d\varepsilon_1+\int_0^{\varepsilon_2^t}\sigma_2 d\varepsilon_2+\int_0^{\varepsilon_3^t}\sigma_3 d\varepsilon_3 \tag{1}$$

where ε_1^t, ε_2^t and ε_3^t are the strains per unit volume of rock corresponding to σ_1, σ_2 and σ_3 at any time step t, respectively.

It is assumed that the physical process of rock deformation and failure under TTC is a closed system without heat energy exchange with the external environment. The total strain energy U of rock can be divided into two parts: the elastic strain energy U^e and the dissipated strain energy U^d. The elastic strain energy U^e can be calculated through Eq. (3), the dissipated strain energy U^d can be obtained through Eqs. (2) and (3),[15,30,31] as shown in follows:

$$U=U^e+U^d \tag{2}$$

$$U^e=U_1^e+U_2^e+U_3^e=\int_0^{\varepsilon_1^{et}}\sigma_1 d\varepsilon_1^e+\int_0^{\varepsilon_2^{et}}\sigma_2 d\varepsilon_2^e+\int_0^{\varepsilon_3^{et}}\sigma_3 d\varepsilon_3^e \tag{3}$$

where U_1^e, U_2^e and U_3^e are the elastic strain energy per unit volume of rock corresponding to σ_1, σ_2 and σ_3, respectively. ε_1^{et}, ε_2^{et} and ε_3^{et} are the elastic strains per unit volume of rock corresponding to σ_1, σ_2 and σ_3 at any time step t, respectively.

Fig. 6 shows the time history curves of the complete energy evolution of the Beishan granite under the same TTC stress states. The time history curves of the total strain energy U, total elastic strain energy U^e and total dissipated strain energy U^d and the strain energy U_1, elastic strain energy $U_1{}^e$ and dissipated strain energy $U_1{}^d$ corresponding to σ_1 are shown in Fig. 6a, c, e. The time history curves of the total strain energy U_2, elastic strain energy U_2^e and dissipated strain energy U_2^d corresponding to σ_2 and the total strain energy U_3, elastic strain energy U_3^e and dissipated strain energy U_3^d corresponding to σ_3 are shown in Fig. 6b, d, f. The complete stress–strain curves of the Beishan granite corresponding to the abovementioned stress levels are shown in Fig. 4b, d and Fig. 5c.

Notably, the pre-peak strains corresponding to σ_2 and σ_3 undergo a change: they first increase and then decrease, that is, the strain is not monotonically increasing (Fig. 4 and Fig. 5). The strain and strain energies corresponding to σ_2 and σ_3 during the pre-peak stage transform from loading-induced compression and energy storage to loading-induced dilation and energy dissipation. Therefore, the strain energy values of the Beishan granite corresponding to σ_2 and σ_3 are first positive and then become negative as the test continues (Fig. 6b, d, f). When the difference between σ_2 and σ_3 is large, this change is particularly obvious on the resultant time history curves of strain energy (Fig. 6d).

The strain energy evolution processes of the Beishan granite are basically similar at pre-peak while they are very different at post-peak under different TTC stress states. In general, the pre-peak plastic deformation of the Beishan granite under the above TTC stress states is not remarkable. Therefore, although a certain strain energy dissipation occurs in the Beishan granite during the pre-peak stage, the magnitude is not large. The time history curves of the pre-peak total strain energy U and total elastic strain energy U^e coincide or are parallel. The two curves begin to bifurcate after reaching the stress yield point, decreasing the rate of increase in the total elastic strain energy U^e, while the rate of increase in the total dissipated strain energy U^d increases (Fig. 6a, c, e).

The time history curves of the strain energy at post-peak are complicated due to the formation of macroscopic fractures in Beishan granite. When σ_2 is relatively small, the strain energies corresponding to σ_2 and σ_3 are smaller than that corresponding to σ_1, so the variation trends and differences of the total strain energy U, the total elastic strain energy U^e and the total dissipated strain energy U^d of the Beishan granite at post-peak are similar to the strain energy U_1, the elastic strain energy U_1^e and the dissipated strain energy U_1^d (Fig. 6a). When σ_2 is relatively higher, the strain energies corresponding to σ_2 and σ_3 are relatively higher than that corresponding to σ_1. The higher σ_2 has a great influence on the variation trends and differences of the total strain energy U, the total elastic strain energy U^e and the total dissipated strain energy U^d of the Beishan granite at post-peak compared to the strain energy U_1, the elastic strain energy U_1^e and the dissipated strain energy U_1^d (Fig. 6c). It can be depicted that the variation trend and differences of the total dissipated strain energy U^d of the Beishan granite at post-peak is quite different from the dissipated strain energy in the σ_1 direction (Fig. 6c).

3.3. AE characteristic and AE hypocenter location of the Beishan granite under TTC

Fig. 7a, b show the time history curves of the stress (σ_1), AE count and cumulative AE count and the corresponding failure behaviour of the Beishan granite under σ_2=75 MPa and σ_3=5 MPa. Fig. 7c, d show the same situations of the Beishan granite under σ_2=150 MPa and σ_3=5 MPa. The maximum AE count of the Beishan granite in Fig. 7a and Fig. 7c are occurred at the stress peak points and are 18222 and 32320, respectively. The cumulative AE count at pre-peak are 74415 and 1043990, respectively; however, they are 1649305 and 18910927 at the end of the test, respectively. The comparison shows that when σ_3 is constant (σ_3=5 MPa) and σ_2=150 MPa, the AE count and cumulative AE count of the Beishan granite are considerably higher than those under σ_2=75 MPa. From the perspective of AE, more severe brittle failure characteristics can be observed at higher σ_2 values, the AE count and cumulative count increase even by a magnitude (Fig. 7a, c). Meanwhile, when σ_2=150 MPa, the Beishan granite exhibits only one macroscopic fracture surface dominated by tensile failure (Fig. 7b). When σ_2=75 MPa, the Beishan granite exhibits two macroscopic fracture surfaces, many secondary micro-cracks are also observed near the main fracture surfaces (Fig. 7d). This trend also indicates that the brittle fracture characteristics of the Beishan granite become more obvious with increasing σ_2.

When σ_2=75 MPa, the number of macroscopic fracture surfaces and micro-cracks in the Beishan granite are much greater than those when σ_2=150 MPa. However, when σ_2=75 MPa, the overall AE activity in the Beishan granite is lower than that when σ_2=150 MPa. This may be because when σ_2 is higher, the brittle failure of rock is more intense, the time from localized failure to macroscopic fracture of rock is relatively short, thus the rate of crack propagation is relatively high. Although the number of macroscopic fracture and micro-cracks is relatively small, the overall intensity and amplitude of the AE signal are relatively higher during rock fracturing, which increases the overall AE activity of the Beishan granite.

Fig. 7e, f show similar conditions as Fig. 7a, b of the Beishan granite when σ_2=75 MPa and σ_3=20 MPa. The maximum AE count of the Beishan granite in Fig. 7a and Fig. 7e are occurred at the peak stress point and the post-peak maximum stress drop point and are 18222 and 15489, respectively. The pre-peak cumulative AE count are 74415 and 416212, respectively; however, they are 1649305 and 4527006 at the end of the test, respectively. When σ_2 is constant (σ_2=75 MPa) and σ_3=20 MPa, the maximum AE count of the Beishan granite is slightly lower than that when σ_3=5 MPa. However, the cumulative AE count at σ_3=20 MPa is greater than that at σ_3=5 MPa, both at pre-peak and at the end of the test (Fig. 7a, e). It can be found that when σ_3=20 MPa, the number of macroscopic fracture surfaces and micro-cracks in the Beishan granite is considerably higher than that when σ_3=5 MPa (Fig. 7b, f). This is because when σ_3 is higher, the time from localized failure to macroscopic fracture of rock is relatively longer, thus the micro-cracks are more developed and more cracks are produced. Therefore, with more AE signals are generated by rock cracking, the cumulative AE count increase.

Fig. 8 shows the fracturing evolution of the Beishan granite based on an analysis of the AE hypocenter location under TTC (σ_2=75 MPa, σ_3=20 MPa) at different times and stress levels. Fig. 8h shows the fracture morphology characteristics and the reference coordinate system of the Beishan granite during final failure. Comparing the actual crack distributions (Fig. 8f, j) of the rock along plane ABCD and plane A`B`C`D` (Fig. 8h) and the corresponding AE hypocenter location results (Fig. 8g, i) shows that the two results are very consistent, which indicates that the AE hypocenter location results can accurately reflect the fracture morphology characteristics and fracture evolution during the final failure of the rock.

Fig. 8a, b, c, d, e show the AE hypocenter location results of the Beishan granite at 365 s, 595 s, 1250 s, 1625 s and 3348 s corresponding to 43 %, 71 %, 100 %, 88 % and 37 % of the peak stress, respectively. Influenced by the composition and microstructure of the Beishan granite and the loading boundary conditions, different damage accumulations form a complex and variable rock fracturing process. According to the difference in damage evolution and accumulation in the rock, the AE hypocenter location results in the four elliptical regions in Fig. 8 are divided into three types, distinguished by three colours: red, blue and green. The analysis of these three typical damage evolution and accumulation processes of the Beishan granite under the given TTC stress state (σ_2=75 MPa, σ_3=20 MPa) is shown as follows:

(1) Fig. 8a-e show that when the rock is under 43 %, 71 %, and 100 % of the peak stress (Fig. 8a-c), there are almost no AE hypocenter location points in the blue elliptical region of the lower left and upper right corners of the rock specimen. When the stress decreases from 100 % to 88 % of the peak stress (Fig. 8d), more AE hypocenter location points are concentrated in the blue elliptical region, and until the final failure of the rock specimen (Fig. 8e), the AE hypocenter location points in this region only slightly increase. Therefore, in practice, the lower left and upper right corners of the rock specimen along the X-Y plane (Fig. 8f, j) are not destroyed before the stress peak is reached, but sudden fracturing occurs in these areas during the first post-peak stress drop. This behaviour may be due to the sudden change in the stress rate and strain rate during the stress drop process, amplifying the stress concentration effect between the edge angle of the rock specimen and the rigid indenter and leading to a final and sudden failure of the rock.

(2) The AE hypocenter location points in the red elliptical region in Fig. 8a-e show a random and irregular scattering from the early loading (Fig. 8a), and the number of AE hypocenter location points in this region grows with the rises of stress up to the rock macro fracturing or overall failure (Fig. 8e). This process indicates that with the incremental change in stress state, the micro-cracks of the rock in this area transform from a random irregular distribution to gradually aggregating along an internal fracture surface, which then gradually coalesces to form a macroscopic fracture surface. This process generally results in the progressive formation of complex fractured bands or regions consisting of multiple macroscopic fractures and micro-cracks.

(3) Unlike the above two regions, the green elliptical region in Fig. 8a-e does not exhibit AE hypocenter location points when the rock is under only 43 % of the peak stress (Fig. 8a). A small number of AE hypocenter location points begin to appear in the green elliptical region when the rock is under 71 % of the peak stress (Fig. 8b), which indicates the development of micro-cracking inside the rock. When the rock is under 100 % of the peak stress (Fig. 8c), the AE hypocenter location points increase and concentrate at the tip of the green fracture surface, as shown in Fig. 8h. When the stress decreases from 100 % to 88 % of the peak stress (Fig. 8d), a large number of AE hypocenter location points concentrating near the macroscopic fracture surface appear in the

green elliptical region, and the macroscopic fracture surface is basically throughgoing. Then, the AE hypocenter location points in this region only increase in number and do not change the overall shape and trend of the macroscopic fracture surface. Unlike the above two cases, the crack initiation and propagation within the green elliptical region is relatively quick, and fractures will quickly penetrate the rock specimen, representing a failure behaviour between sudden failure and progressive failure.

4. Discussion

4.1. Fracturing process analysis combining the AE and strain energy characteristic parameters

The rock fracturing can be precisely captured by AE and it is also a energy evolution process.[15,18] Hence, the entire fracturing process of the Beishan granite under TTC is studied by combining AE and strain energy characteristics in this section. Fig. 9 shows the complete fracturing process of the Beishan granite under TTC (σ_2=75 MPa, σ_3=20 MPa) in terms of the AE and strain energy characteristics. The time history curves of σ_1, the AE and strain energy parameters are shown in Fig. 9a-e. Additionally, according to the different damage evolution and accumulation processes, the complete stress–strain curve under TTC (Fig. 9a) can be divided into five stages: micro-cracks closure (OA), elastic deformation (AB), stable propagation of micro-cracks (BC), accelerated extension of cracks (CD) and post-peak strength loss and residual shearing (DE).

During the micro-cracks closure stage (OA), the original micro-cracks and micro-defeats of the rock are compacted and closed, and the internal particles become interlocked. Therefore, a small number of AE signals are generated at this stage, and the AE count and the cumulative AE count are relatively low (Fig. 9a). The AE amplitude is also generally low (less than 50 dB), mostly near the detection threshold (45 dB) (Fig. 9b). During this stage, the energy is input by the testing machine through compressing and working on the rock, and most of the input energy is transformed into elastic strain energy and stored. Only a small amount of the energy is dissipated by the compaction of original micro-cracks and the interaction of particles inside the rock. The total elastic strain energy and total dissipated strain energy are both very low (Fig. 9c, d), but the strain energy ratio curves change very sharply. The ratio of total elastic strain energy decreases rapidly to a minimum, while the ratio of the total dissipated strain energy increases rapidly to a maximum (Fig. 9e).

During the elastic deformation stage (AB), very few micro-cracks events occur in the rock, AE activity is in a quiet period, the AE count and the cumulative AE count remain very low (Fig. 9a) The AE amplitude is relatively low, generally lower than 50 dB (Fig. 9b). During this stage, all the work done by the testing machine is transformed into elastic strain energy in the rock, which is the main energy storage stage of the rock. Therefore, the total elastic strain energy continuously increases, while the total dissipated strain energy remains unchanged (Fig. 9c, d). The ratio of total elastic strain energy continuously increases, while the ratio of total dissipated strain energy continuously decreases (Fig. 9e).

After loading to the stable propagation of micro-cracks stage (BC), the micro-cracks initiate and propagate steadily. Consequently, AE activity gradually increases, and the AE count and cumulative AE count also increase, but the values are not high (Fig. 9a). The AE amplitude continuously increases but is still lower than 70 dB (Fig. 9b). In this stage, because of the stable propagation of micro-cracks in the rock, the energy input by the testing machine is partly transformed into elastic strain energy and partly transformed into dissipated strain energy, but the elastic strain energy in the rock is still dominant (Fig. 9c, d). The total elastic strain energy ratio continues to increase, but the rate of increase decreases, and a maximum total elastic strain energy ratio is reached at the end of this stage. The variation in the total dissipated strain energy ratio is opposite to that of the total elastic strain energy ratio (Fig. 9e).

During the stage of accelerated extension of cracks (CD), the micro-cracks propagate rapidly and consequently AE event activity increases significantly. The AE count increases rapidly and it has a sharply increases at the peak stress point. The cumulative AE count shows dramatic increases and its curve increases rapidly (Fig. 9a). The AE amplitude increases rapidly, and its maximum value is approximately 100 dB (Fig. 9b). During this stage, the total elastic strain energy decreases, and the total dissipated strain energy increases due to the accelerated propagation of the micro-cracks in the rock (Fig. 9c, d). Additionally, the total elastic strain energy ratio begins to decrease, and the total dissipated strain energy ratio begins to increase (Fig. 9e).

Finally, in the post-peak strength loss and residual shearing stage (DE), a large number of micro-cracks inside the rock rapidly aggregate and form macroscopic failure surfaces. Meanwhile, the AE event activity is extremely frequent and active. The AE count is relatively high and reaches its maximum value at the maximum post-peak stress drop point. The cumulative AE count increases rapidly and a sudden jump occurs at the maximum post-peak stress drop point (Fig. 9a). The AE amplitude generally remains above 70 dB, and the maximum AE amplitude is approximately 100 dB (Fig. 9b). During this stage, the total elastic strain energy decreases rapidly and the total dissipated strain energy increases rapidly due to the stored elastic strain energy is released quickly (Fig. 9c, d). The total elastic strain energy ratio decreases rapidly, while the total dissipated strain energy ratio increases rapidly (Fig. 9e).

It is worth mentioning that the damage stress threshold (σ_{cd}) of the rock can be determined by a maximum value of the elastic strain energy ratio or a minimum value of the dissipated strain energy ratio (Fig. 9e). The damage stress threshold (σ_{cd}) defined in Fig. 9e is also the starting point of the bifurcation between the total strain energy curve and the total elastic strain energy curve of the rock (Fig. 9c). Clearly, this point is point C, which represents the start of the accelerated extension of cracks stage (CD). Besides, the damage stress threshold point (σ_{cd}) is also corresponding to the maximum AE count within the blue circle (Fig. 9a). Starting at the accelerated extension of cracks stage (point C), the crack propagation rate increases rapidly, and the AE count responds by suddenly increasing. This may be that a sudden increase in the rate of crack propagation causes high-frequency vibration signals to be released from the micro-crack tips, leading to an increase in the number of oscillations of the monitored AE voltage signal, exceeding the threshold voltage and creating a local peak in the AE count.

4.2. Fracturing process analysis combining the AE hypocenter location and strain energy

The AE hypocenter location results of the Beishan granite under TTC (σ_2=75 MPa, σ_3=20 MPa) are shown by the stress–time curve (Fig. 10a) and stress–strain curve (Fig. 10b). The reference coordinate system used to analyse the fracturing process in Fig. 11 is shown with the specimen model in Fig. 10a. The total duration time of the TTC and AE test is 0.93 h (Fig. 10 and Fig. 11). Corresponding to Fig. 11a-h, the increments of the AE count S_c, AE event S_e and the total elastic strain energy U_e per unit time ($\Delta S_c/\Delta t$, $\Delta S_e/\Delta t$ and $\Delta U_e/\Delta t$) and the increments of the total elastic strain energy (ΔU_e) shown in Fig. 11i, j can be solved according to the following Eqs. (4), (5), (6) and (7):

$$\frac{\Delta S_c}{\Delta t} = \frac{S_c^i - S_c^{i-1}}{t^i - t^{i-1}} \tag{4}$$

$$\frac{\Delta S_e}{\Delta t} = \frac{S_e^i - S_e^{i-1}}{t^i - t^{i-1}} \tag{5}$$

$$\frac{\Delta U_e}{\Delta t} = \frac{U_e^i - U_e^{i-1}}{t^i - t^{i-1}} \tag{6}$$

$$\Delta U_e = U_e^i - U_e^{i-1} \tag{7}$$

Where $i = 1, 2, \ldots, 8$; $t^0 = 0\ \text{s},\ t^1 = 365\ \text{s}, \ldots,\ t^8 = 3348\ \text{s}$; $S_c^0 = 0,\ S_c^1 = 734, \ldots,\ S_c^8 = 472000$; $S_e^0 = 0,\ S_e^1 = 25, \ldots,\ S_c^8 = 9612$; $U_e^0 = 0\ \text{kJ/m}^3,\ U_e^1 = 304\ \text{kJ/m}^3, \ldots,\ U_e^8 = 233\ \text{kJ/m}^3$.

As shown in Fig. 11a-h, during the initial loading stage, the AE event representing the micro-cracking are randomly scattered over the specimen. With increasing loading, the AE event gradually increase and concentrate near the fracture surfaces inside the rock, finally forming a macroscopic fracture zone. It can be found that when the stress of the rock increases from 43 % to 92 % of the peak stress, the increase in stress is as high as 49 %, and the number of AE event increases by 474 (Fig. 11a, c); however, when the stress level of the rock increases from 92 % to 100 %, the increase in stress is only 8 %, and the number of AE event increases by 1141 (Fig. 11c, d). Meanwhile, the $\Delta S_c/\Delta t$ and $\Delta S_e/\Delta t$ are considerably low before 92 % of the peak stress. While their magnitudes rapidly increase and their curve slopes increase significantly when the stress is increased from 92 % to 100 % of the peak stress (Fig. 11i). As shown in Fig. 11j, although the $\Delta U_e/\Delta t$ shows reduction after 71 % of the peak stress, the ΔU_e increases until 92 % of the peak stress. After 92 % of the peak stress, The ΔU_e and $\Delta U_e/\Delta t$ decrease appreciably due to the significant increase of the cracking and energy dissipation inside the rock.

Through the above analysis, we found that the AE activity of the micro-cracking of the Beishan granite is not very active before 92 % of the peak stress. When the stress is as high as 92 % of the peak stress, a lot of micro-cracks form and develop in the rock specimen, thus the AE activity becomes very active. Clearly, for hard brittle rocks such as Beishan granite, when the stress does not reach a very high level, few micro-cracks form in the rock and their AE activity is low. Only when the stress reaches a high level or approaches the peak stress, the micro-cracks inside the rock suddenly increase, leading to instability and failure of the rock in a short time, which reveals the reason why the rockburst of deep hard rock mass is in a sudden failure.

To analyse the post-peak fracturing processes of the Beishan granite, it can be seen that when the stress drop of the rock is only 12 % (from 100 % of the peak stress to 88 %) and 10 % (from 88 % of the peak stress to 78 %) of the peak stress, the increments of the AE event are as high as 4762 and 3194 (Fig. 11d, e, f); however, when the stress drop of rock is as high as 41 % (from 78 % of the peak stress to 37 %), the increment of the AE event is only 16 (Fig. 11f, h). As shown in Fig. 11i, the $\Delta S_c/\Delta t$ and $\Delta S_e/\Delta t$ increase rapidly when the rock stress decreases from 100 % to 88 % of the peak stress. While the $\Delta S_c/\Delta t$ and $\Delta S_e/\Delta t$ decrease rapidly when the rock stress decreases from 88 % to 78 % of the peak stress and from 78 % to 37 % of the peak stress. Moreover, it also can be found that the former change (88 % to 78 %) is greater than the latter change (78 % to 37 %) in terms of the reduction in magnitude and curve slope. In term of the strain enegy, during the first post-peak stress drop process (from 100 % to 88 % of the peak stress), the ΔU_e and $\Delta U_e/\Delta t$ decrease continuously and their curve slopes also decrease. While during the second post-peak stress drop process (from 88 % to 78 % of the peak stress), the stress–strain curve has a process of slightly rising and then falling (Fig. 10b), thus both the elastic strain energy storage and release occur inside the rock during this process. Eventually, the $\Delta U_e/\Delta t$ increases slightly while the ΔU_e remains basically unchanged. When the stress drops from 78 % to 37 % of the peak stress (test termination point), due to the formation of the rock macroscopic fracture, the changes in the ΔU_e and $\Delta U_e/\Delta t$ are not large and their curve slopes are relatively gentle.

Through the above analyses, it can be found that the formation of macroscopic fractures and the rapid release of elastic strain energy stored in the rock mostly occur during the first stress drop process. Meanwhile, the maximum values of $\Delta S_e/\Delta t$, ΔU_e and $\Delta U_e/\Delta t$ all occur during this process. Therefore, for hard brittle rocks such as Beishan granite, once macroscopic fracturing occurs, the strain energy in the rock will rapidly release and produce numerous AE event. Meanwhile, with the further developing of the rock macroscopic fracturing, the post-peak fracturing of hard rock can be more severe and difficult to control and ultimately leads to the strength loss and instability failure of the rock. The findings are helpful to reveal and understand why the process of rockburst in the hard rock is often very intense and uncontrollable.

5. Conclusion

In this paper, the TTC and AE tests of the Beishan granite are performed. The stress–strain relationship, AE and strain energy characteristics of the Beishan granite under TTC conditions are studied. The fracture process of the Beishan granite is illustrated with deep insight by combining the AE and strain energy results. Within the scope of this study, we found that when σ_2 is high, the rock tends to exhibit Class II failure, and its brittle failure is obvious; additionally, the overall AE activity is more intense, increasing the AE count and cumulative AE count. The damage evolution and accumulation in the rock are identified into three types according to the AE hypocenter location results. The strain energy variations of the Beishan granite at pre-peak are basically similar while they are quite different at post-peak especially when σ_2 is high. By integrating AE and strain energy results, five fracturing evolution stages of the Beishan granite are discussed. Damage stress threshold (σ_{cd}) can be determined by a maximum value of the elastic strain energy ratio or a minimum value of the dissipated strain energy ratio. For the hard brittle rocks such as Beishan granite, only when the stress approaches the peak stres, the micro-cracks inside the rock will increase suddenly and lead to a rapid instability and failure. Once macroscopic fracturing occurs during the post-peak stage, the rapid energy release will lead to further violent fracturing.

Acknowledgements

This study was supported by the 111 Project (No. B17009), the CAS Key Research Program of Frontier Sciences (No. QYZDJ-SSW-DQC016), and the National Natural Science Foundation, China (No. 51579043, 51709043).

References

1. Feng XT, Hudson JA. Rock Engineering Design. CRC Press; 2011.
2. Feng XT, Zhang XW, Kong R, Wang G. A novel mogi type true triaxial testing apparatus and its use to obtain complete stress–strain curves of hard rocks. Rock Mech Rock Eng. 2016;49(5):1649–1662.
3. Zhao J, Feng XT, Zhang XW, Zhang Y, Zhou YY, Yang CX. Brittle-ductile transition and failure mechanism of Jinping marble under true triaxial compression. Eng Geol 2018;232:160–170.
4. Kong R, Feng XT, Zhang XW, Yang CX. Study on crack initiation and damage stress in sandstone under true triaxial compression. Int J Rock Mech Min Sci. 2018;106:117–123.
5. Lockner DA. The role of acoustic emission in the study of rock failure. Int J Rock Mech Min Sci and Geomech Abstr. 1993;30(7):883–899.
6. Rück M, Rahner R, Sone H, Dresen G. Initiation and propagation of mixed mode fractures in granite and sandstone. Tectonophysics. 2017;717:270–283.
7. Kaiser EJ. A study of acoustic phenomena in tensile test. Doctoral thesis. Technische Hochschule München, Munich, Germany; 1959.

8. Ohtsu M. Simplified moment tensor analysis and unified decomposition of acoustic emission source: Application to in situ hydrofracturing test. J Geophys Res. 1991;96(B4):6211–6221.
9. Zang A, Wagner FC, Stanchits S, Dresen G, Andresen R, Haidekker MA. Source analysis of acoustic emissions in Aue granite cores under symmetric and asymmetric compressive loads. Geophys J Int. 1998;135:1113–1130.
10. Thompson BD, Young RP, Lockner DA. Observations of premonitory acoustic emission and slip nucleation during a stick slip experiment in smooth faulted Westerly granite. Geophys Res Lett. 2005;32, L10304.
11. Moradian Z, Einstein HH, Ballivy G. Detection of cracking levels in brittle rocks by parametric analysis of the acoustic emission signals. Rock Mech Rock Eng. 2016;49(3):785–800.
12. Gong YX, Song ZJ, He MC, Gong WL, Ren FQ. Precursory waves and eigenfrequencies identified from acoustic emission data based on Singular Spectrum Analysis and laboratory rock-burst experiments. Int J Rock Mech Min Sci. 2017;91:155–169.
13. Lei XL, Nishizawa O, Kusunose K, Cho A, Satoh T, Nishizawa O. Compressive failure of mudstone samples containing quartz veins using rapid AE monitoring: the role of asperities. Tectonophysics. 2000;328(3):329–340.
14. Stanchits S, Mayr S, Shapiro S, Dresen G. Fracturing of porous rock induced by fluid injection. Tectonophysics. 2011;503(1):129–145.
15. Xie HP, Li LY, Peng RD, Ju Y. Energy analysis and criteria for structural failure of rocks. J Rock Mech Geotech Eng. 2009;1:11–20.
16. Chen ZQ, He C, Wu D, Xu GW, Yang WB. Fracture evolution and energy mechanism of deep-buried carbonaceous slate. Acta Geotech. 2017;12:1243–1260.
17. Hua AZ, You MQ. Rock failure due to energy release during unloading and application to underground rock burst control. Tunn Undergr Sp Technol. 2013;23(8):1572–1578.
18. Li DY, Sun Z, Xie T, Li XB, Ranjith PG. Energy evolution characteristics of hard rock during triaxial failure with different loading and unloading paths. Eng Geol. 2017;228:270–281.
19. Tarasov BG, Stacey TR. Features of the energy balance and fragmentation mechanisms at spontaneous failure of class I and class II rocks. Rock Mech Rock Eng. 2017;50(10):2563–2584.
20. Zhang J, Ai C, Li YW, Che MG, Gao R, Zeng J. Energy-based brittleness index and acoustic emission characteristics of anisotropic coal under triaxial stress condition. Rock Mech Rock Eng. 2018;51:3343–3360.
21. Abu Al-Rub RK, Voyiadjis GZ. On the coupling of anisotropic damage and plasticity models for ductile materials. Int J Solids Struct. 2003;40(2):2611–2643.
22. Wang J. High-level radioactive waste disposal in China: update 2010. J Rock Mech Geotech Eng. 2010;2(1):1–11.
23. Zhao XG, Cai M, Wang J, Ma LK. Damage stress and acoustic emission characteristics of the Beishan granite. Int J Rock Mech Min Sci. 2013;64:258–269.
24. Feng XT, Zhang XW, Yang CX, Kong R, Liu XY, Peng S. Evaluation and reduction of the end friction effect in true triaxial tests on hard rocks. Int J Rock Mech Min Sci. 2017;97:144–148.
25. Haimson BC, Chang C. A new true triaxial cell for testing mechanical properties of rock, and its

use to determine rock strength and deformability of Westerly granite. Int J Rock Mech Min Sci. 2000;37(1):285–296.

26. Du K, Tao M, Li XB, Zhou J. Experimental study of slabbing and rockburst induced by true-triaxial unloading and local dynamic disturbance. Rock Mech Rock Eng. 2016;49(9):1–17.
27. Solecki R, Conant R J. Advanced mechanics of materials. London: Oxford University Press; 2003.
28. Huang D, Li YR. Conversion of strain energy in triaxial unloading tests on marble. Int J Rock Mech Min Sci. 2014;66:160–168.
29. Ning JG, Wang J, Jiang JQ, Hu SC, Jiang LS, Lu XS. Estimation of crack initiation and propagation thresholds of confined brittle coal specimens based on energy dissipation theory. Rock Mech Rock Eng. 2018;51:119–134.
30. Jaeger JC, Cook NGW, Zimmerman RW. Fundamentals of Rock Mechanics (4th Edition). Wiley-Blackwell; 2007.
31. Peng RD, Ju Y, Wang JG, Xie HP, Gao F, Mao LT. Energy dissipation and release during coal failure under conventional triaxial compression. Rock Mech Rock Eng. 2015;48(2):509–526.

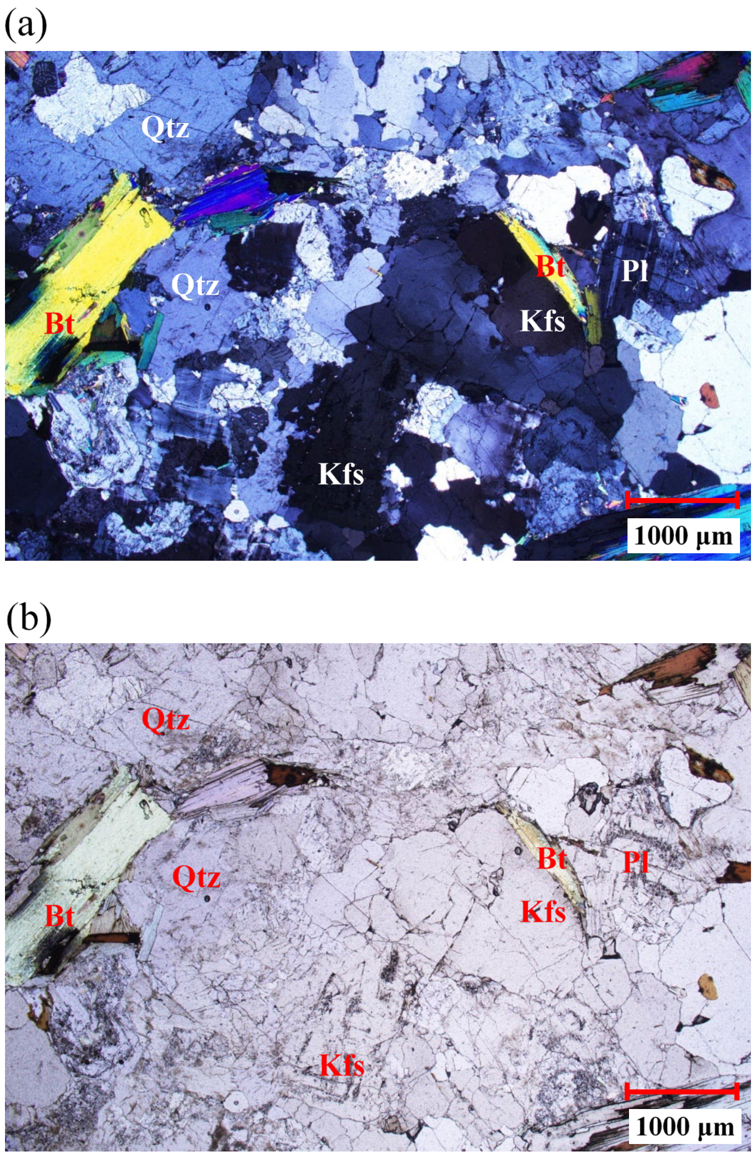

Fig. 1. Optical micrograph of Beishan granite showing the textures of major rock and ore types, with major crystals of quartz (Qtz), K-feldspar (Kfs), plagioclase (Pl) and biotite (Bt). (a) Crossed polars. (b) Plane polarized light.

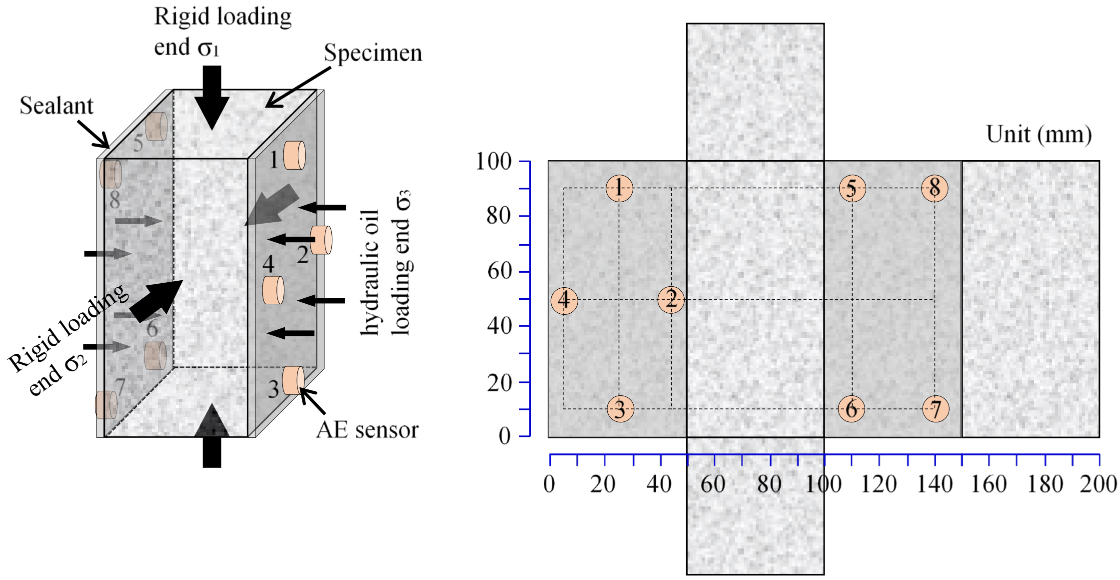

Fig. 2. Illustration of the tested specimen and AE sensors distribution during the true triaxial compression test.

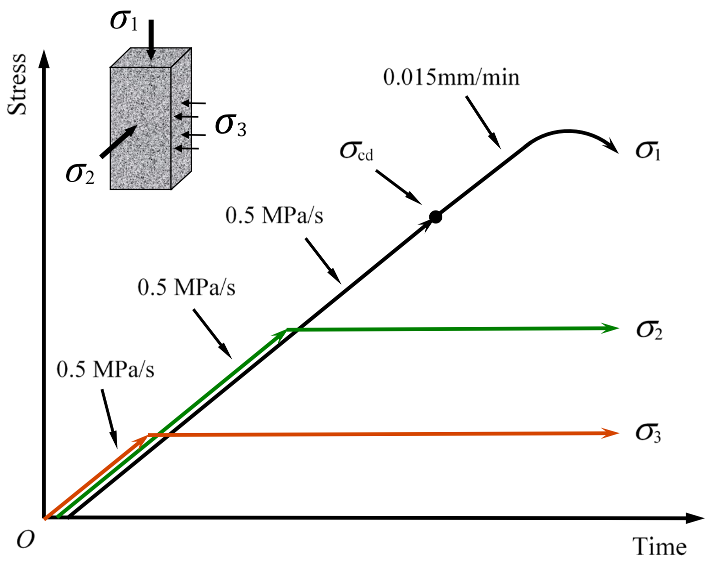

Fig. 3. Stress path applied during the true triaxial experiments.

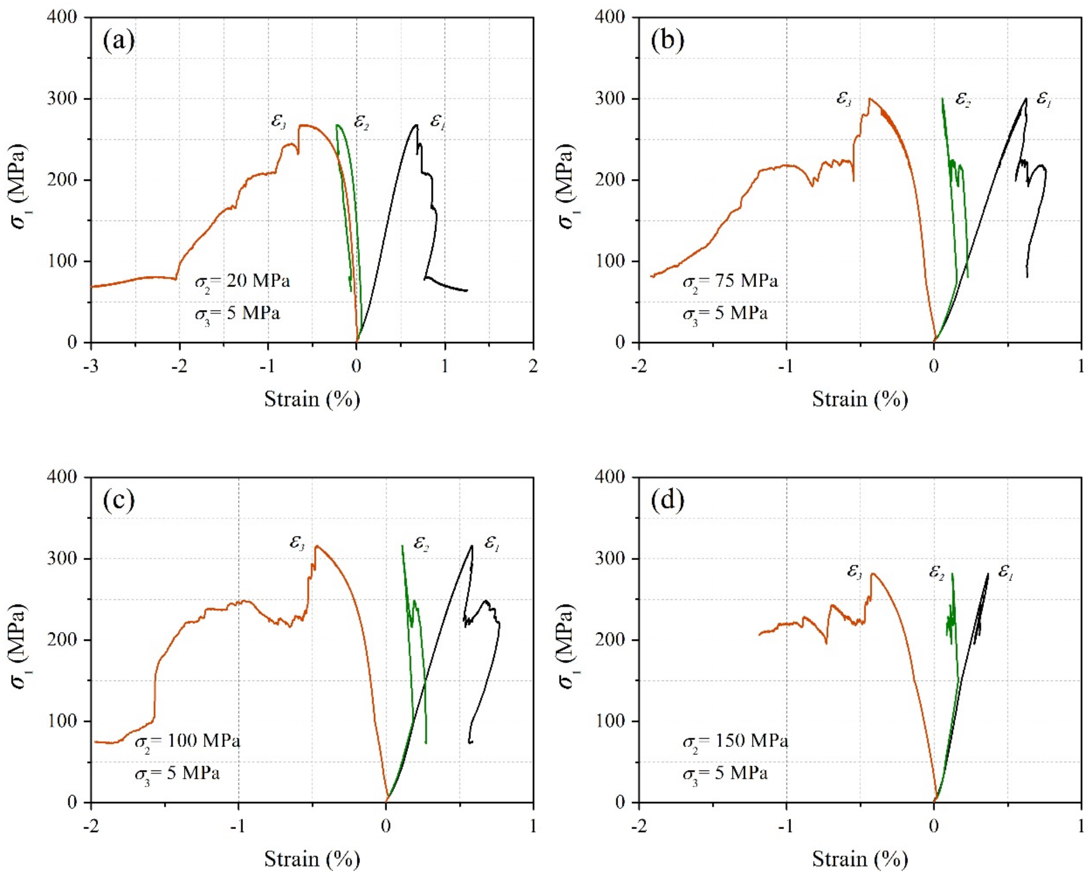

Fig. 4. Stress–strain relationships of Beishan granite at different intermediate principle stress (σ_2) levels and constant minimum principal stress (σ_3) (σ_3=5 MPa) during true triaxial compression. (a) σ_2=20 MPa, σ_3=5 MPa. (b) σ_2=75 MPa, σ_3=5 MPa. (c) σ_2=100 MPa, σ_3=5 MPa. (d) σ_2=150 MPa, σ_3=5 MPa.

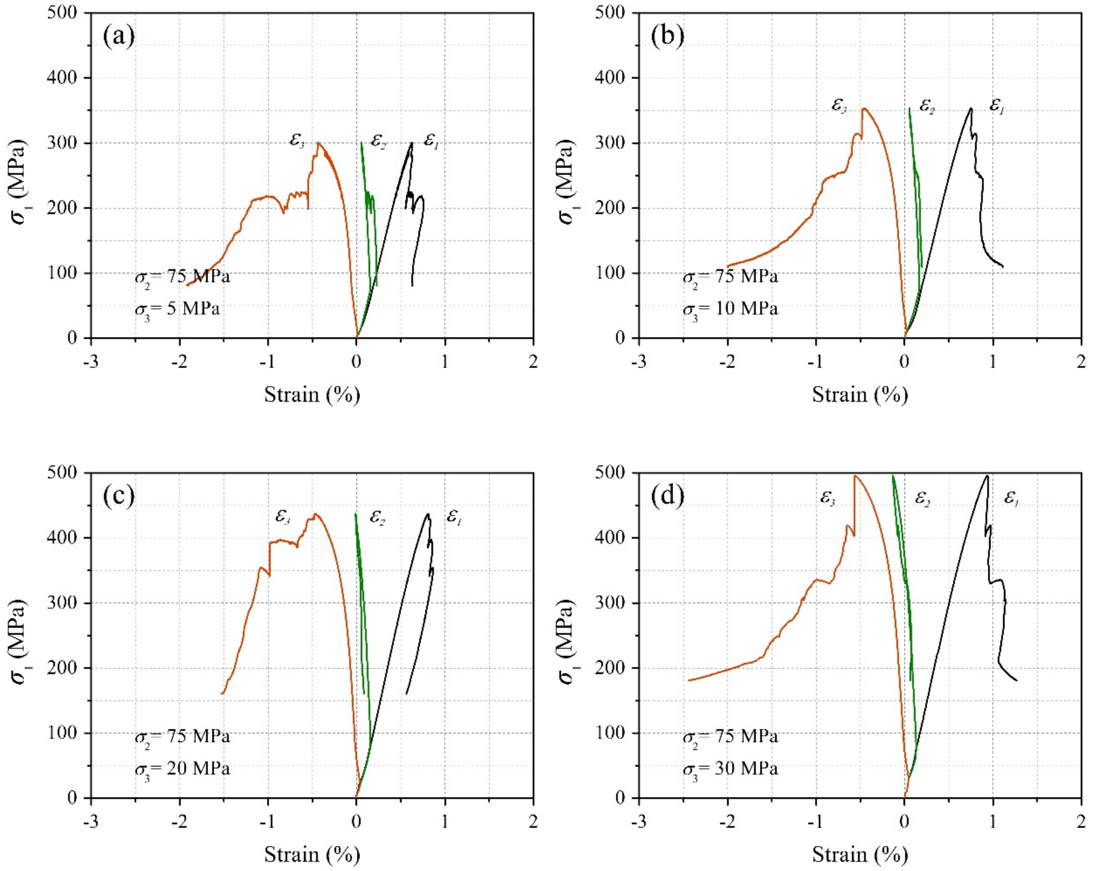

Fig. 5. Stress–strain relationships of Beishan granite at different minimum principal stress (σ_3) levels and constant intermediate principal stress (σ_2) (σ_2=75 MPa) during true triaxial compression. (a) σ_2=75 MPa, σ_3=5 MPa. (b) σ_2=75 MPa, σ_3=10 MPa. (c) σ_2=75 MPa, σ_3=20 MPa. (d) σ_2=75 MPa, σ_3=30 MPa.

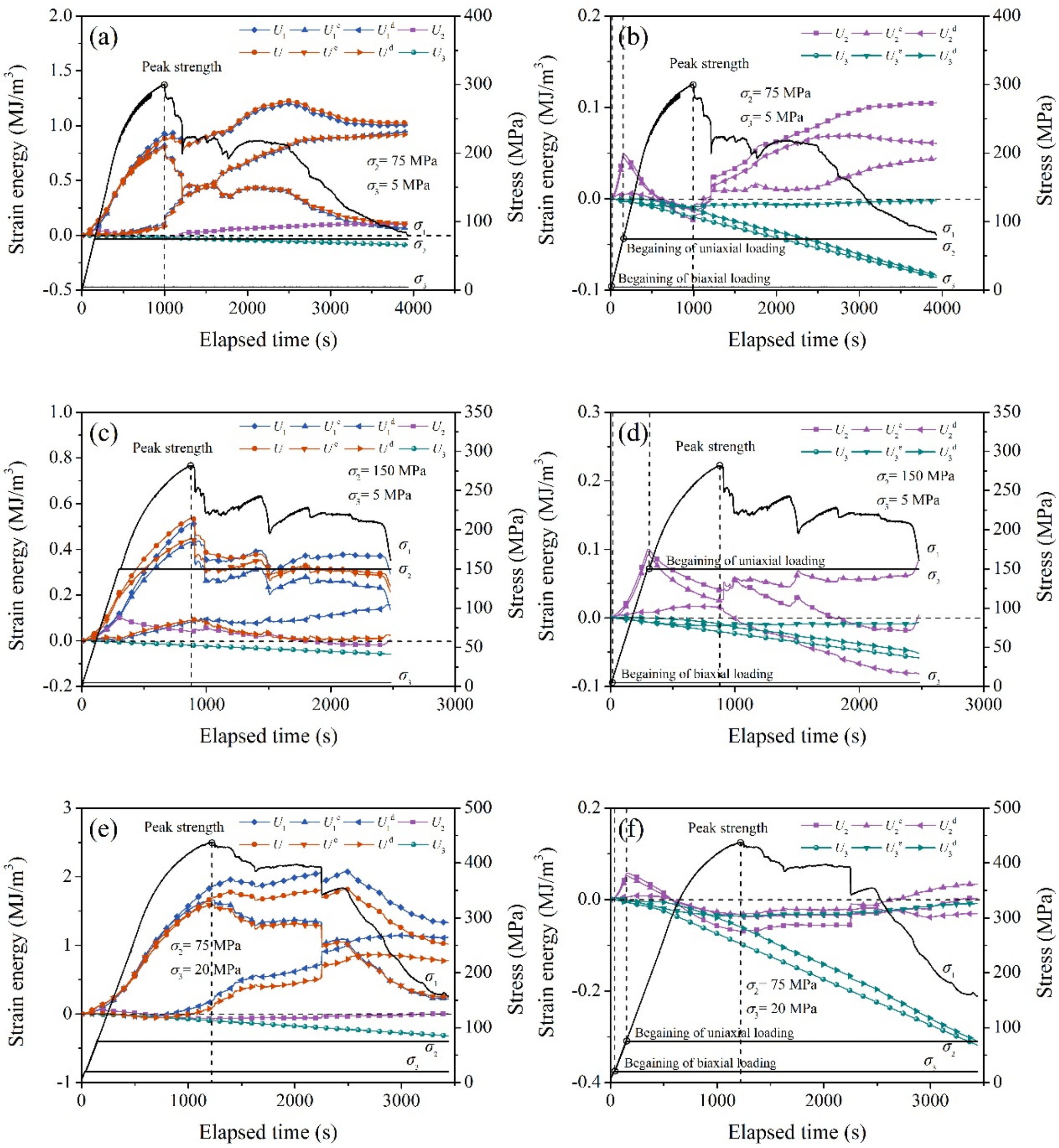

Fig. 6. Strain energy characteristics of Beishan granite during true triaxial compression test. (a) and (b) σ_2=75 MPa, σ_3=5 MPa. (c) and (d) σ_2=150 MPa, σ_3=5 MPa. (e) and (f) σ_2=75 MPa, σ_3=20 MPa.

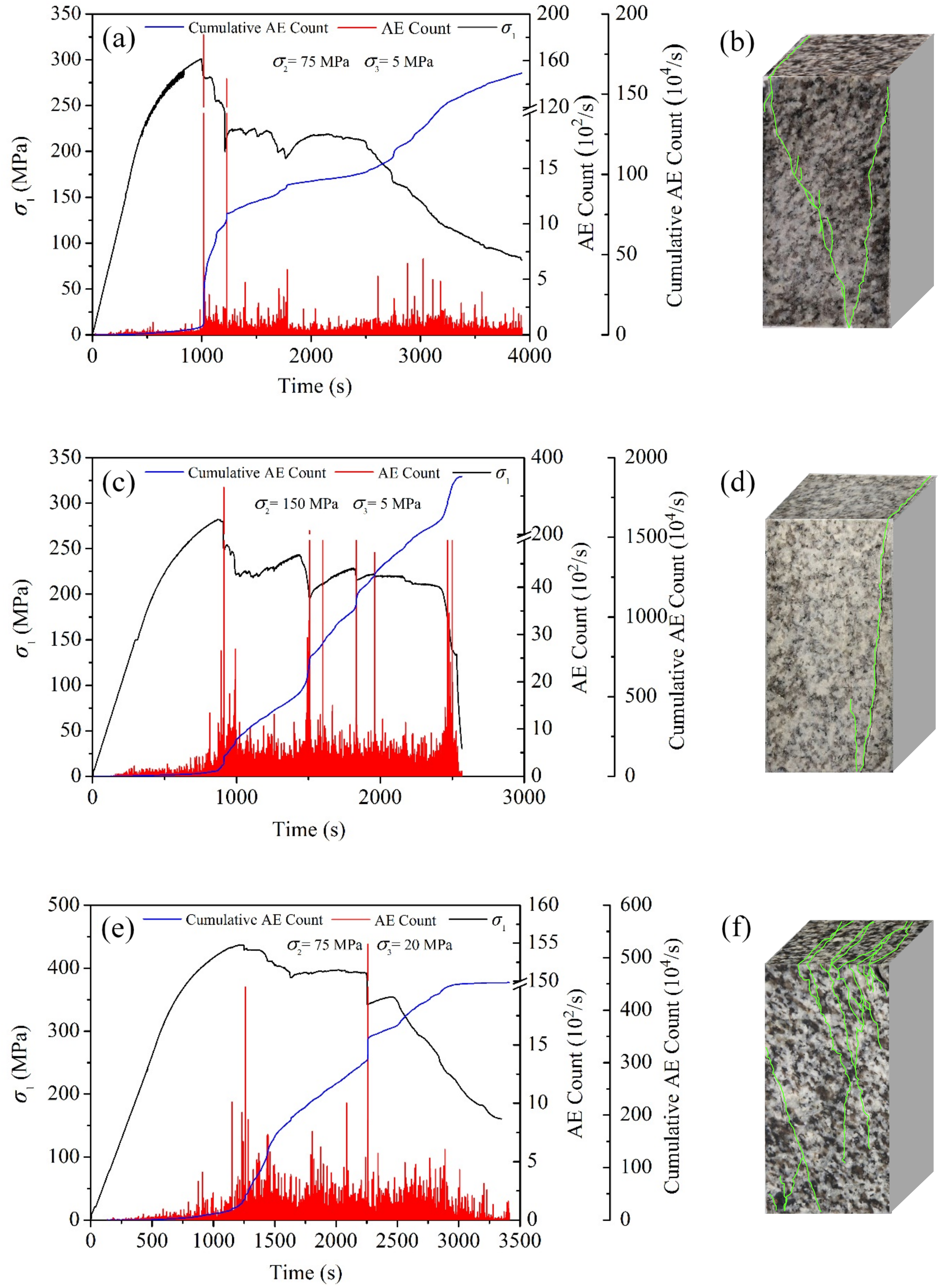

Fig. 7. AE characteristics and failure behaviors of Beishan granite under true triaxial compression. (a) and (b) σ_2=75 MPa, σ_3=5 MPa. (c) and (d) σ_2=150 MPa, σ_3=5 MPa. (e) and (f) σ_2=75 MPa, σ_3=20 MPa.

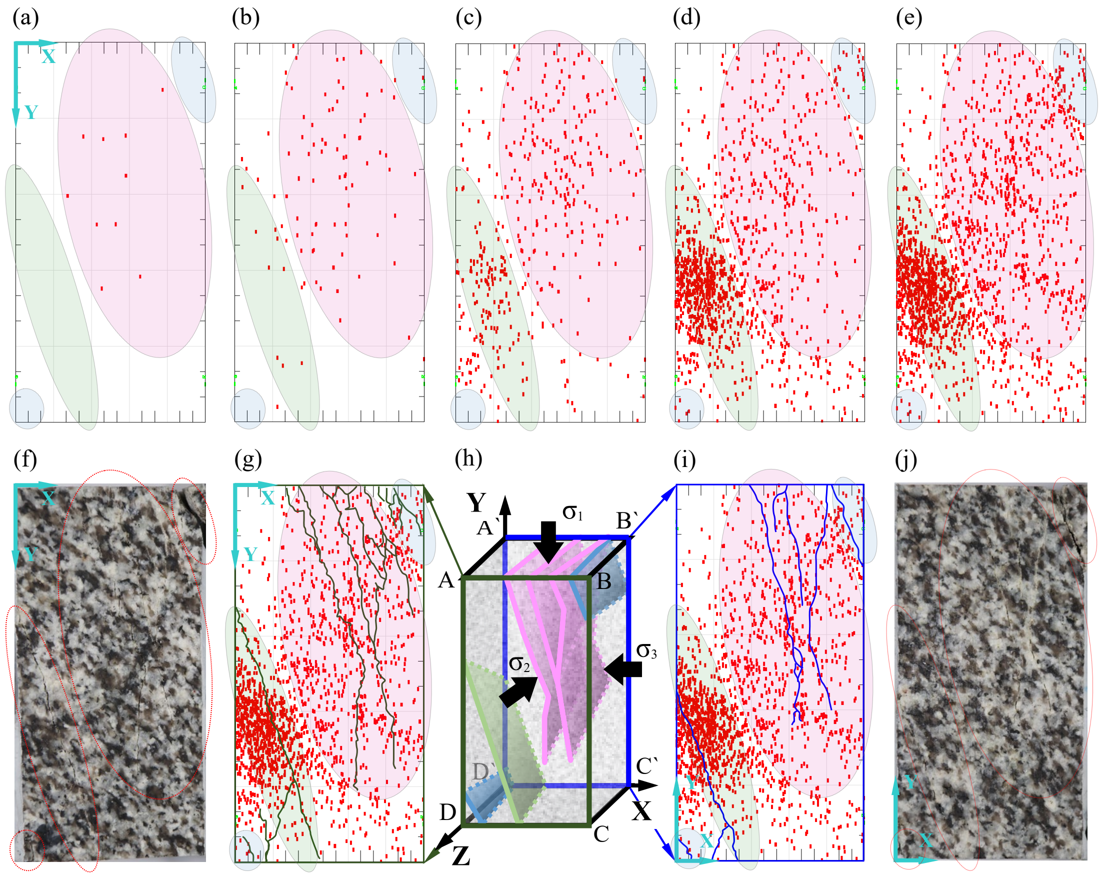

Fig. 8. Fracturing evolution process of Beishan granite based on AE hypocenter location under true triaxial compression (σ_2=75 MPa, σ_3=20 MPa) at different elapsed times and stress levels. (a) 365s, $\sigma_1/\sigma_{1\text{peak}}$=43 %. (b) 595s, $\sigma_1/\sigma_{1\text{peak}}$=71 %. (c) 1250s, $\sigma_1/\sigma_{1\text{peak}}$=100 % (the peak stress point). (d) 1625s, $\sigma_1/\sigma_{1\text{peak}}$=88 % (the first stress-drop point at post-peak). (e) 3348s, $\sigma_1/\sigma_{1\text{peak}}$=37 % (test termination point). (h) Schematic spatial model of fracture morphology of tested rock in reference coordinate system. Corresponding to the different color of ellipse regions in (a-e), spatial failure planes with corresponding color in (h) show the time difference and formation process difference of cracking behavior of tested rock. (f, g) Comparison of actual crack distribution (f) and AE hypocenter location (g) on plane ABCD of the final failure specimen. The morphology and distribution of cracks are depicted on AE hypocenter location map (g) according to the actual fracture characteristics on plane ABCD. (i, g) The case of (i, g) on plane A`B`C`D` is the same as (f, g), (i) is the AE hypocenter location and (j) is the actual crack distribution.

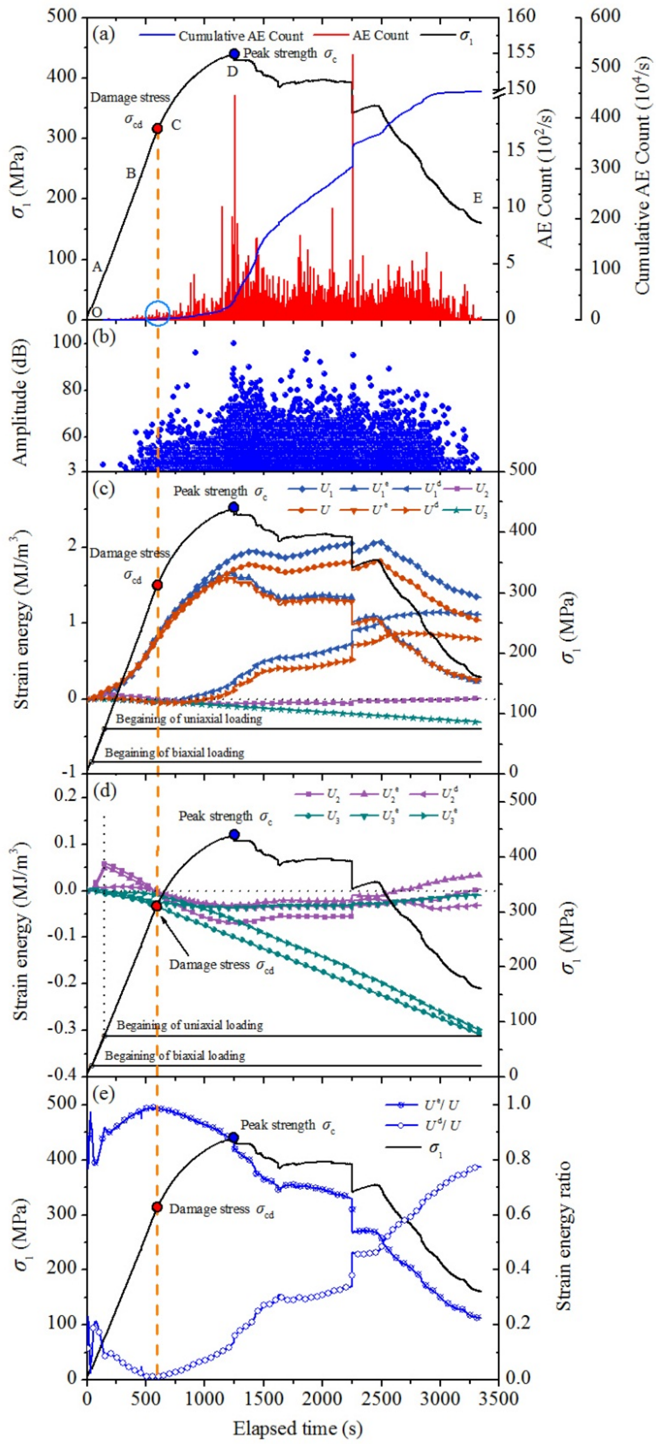

Fig. 9. Complete behavior process of Beishan granite under true triaxial compression associate with AE and strain energy characteristic. The maximum principal stress (σ_1) time history curves of one representative test result with true triaxial stress state of σ_2=75 MPa, σ_3=20 MPa are shown in each subgraph. Additional to time history curves are shown as: (a) AE count (red bars) and cumulative AE count (blue line), (b) amplitude, (c) total strain energies and strain energies at σ_1 direction, (d) strain energies at σ_2 and σ_3 directions, and (e) strain energy ratios.

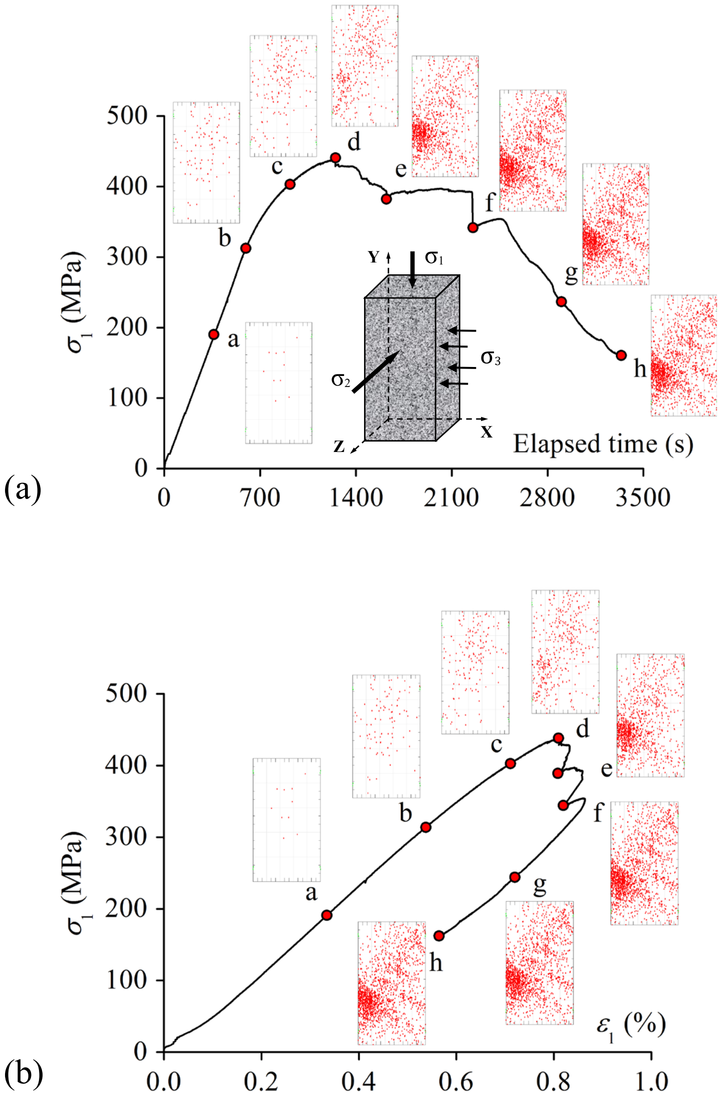

Fig. 10. AE hypocenter location results at selected states during complete behavior process of Beishan granite under true triaxial compression (σ_2=75 MPa, σ_3=20 MPa) corresponds to different (a) elapsed times and (b) stress levels. The time points corresponding to the points a-h are 365 s, 595 s, 916 s, 1250 s, 1625 s, 2250 s, 2880 s and 3348 s, respectively. The stress levels (σ_1/σ_{1peak}) corresponding to the points a-h are 43 %, 71 %, 92 %, 100 % of the peak stress at pre-peak and 88 %, 78 %, 55 %, 37 % of the peak stress at post-peak, respectively.

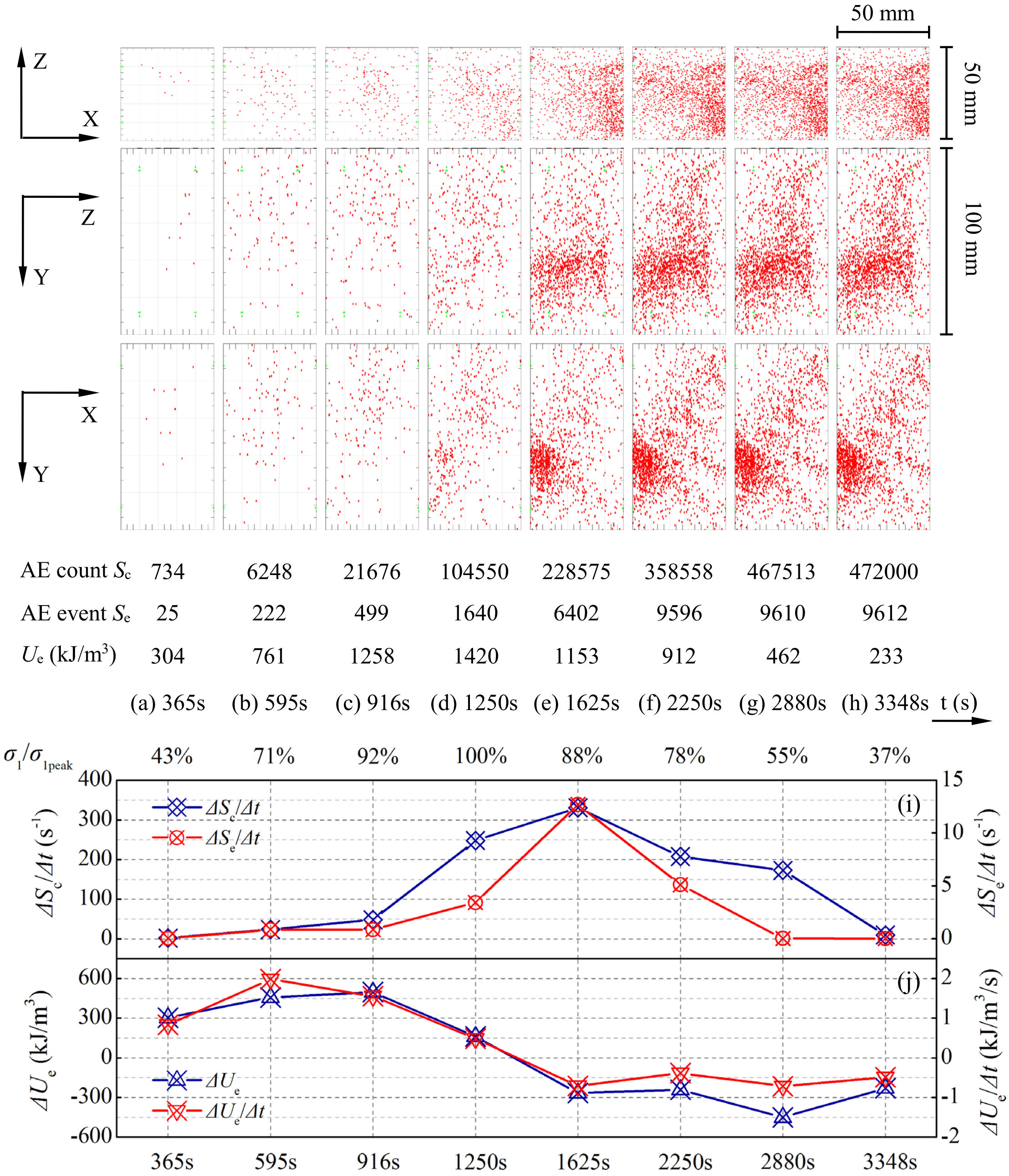

Fig. 11. AE hypocenter location and energy evolution characteristic at different time point of Beishan granite under true triaxial compression (σ_2=75 MPa, σ_3=20 MPa) (total duration 3348 s = 0.93 hour). The reference coordinate system used to analysis in this figure as shown in the Fig. 10a. (a-h) Orthographic views of AE hypocenter location at different elapsed times associate with AE count S_c and AE event S_e. (i) Increments of AE count S_c and AE event S_e per unit time ($\Delta S_c/\Delta t$ and $\Delta S_e/\Delta t$) and (j) increments of total elastic strain energy (ΔU_e) and total elastic strain energy per unit time ($\Delta U_e/\Delta t$) change with different time sections and different stress levels (σ_1/σ_{1peak}).